



Original Research

Nickel-metal-organic framework nanobelt based composite membranes for efficient Sr²⁺ removal from aqueous solutionJunye Cheng^{a, b}, Kaili Liu^{a, c}, Xin Li^a, Lei Huang^d, Jie Liang^{c, *}, Guangping Zheng^b, Guangcun Shan^{a, **}^a School of Instrumentation Science and Opto-electronics Engineering, Beihang University, No.37 XueYuan Road, Beijing, 100083, China^b Department of Mechanical Engineering, The Hong Kong Polytechnic University, Kowloon, Hong Kong, 999077, China^c School of Environment and Space Engineering, Beihang University, Beijing, 100191, China^d School of Metallurgy and Environment, Central South University, Changsha, 410083, China

ARTICLE INFO

Article history:

Received 7 February 2020

Received in revised form

20 April 2020

Accepted 10 May 2020

Keywords:

Metal-organic framework (MOF) nanobelts

Graphene oxide

Radioactive waste

Strontium ions

Adsorption

ABSTRACT

The sorption removal of radionuclides Sr²⁺ using a freestanding functional membrane is an interesting and significant research area in the remediation of radioactive wastes. Herein, a novel self-assembled membrane consisting of metal-organic framework (MOF) nanobelts and graphene oxides (GOs) are synthesized through a simple and facile filtration method. The membrane possesses a unique interwove morphology as evidenced from SEM images. Batch experiments suggest that the GO/Ni-MOF composite membrane could remove Sr²⁺ ions from aqueous solutions and the Sr²⁺ adsorption capacity and efficiency of the GO/Ni-MOF composite membrane is relevant to the MOF content in the composite. Thus, the dominant interaction mechanism was interface or surface complexation, electrostatic interaction as well as ion substitution. The maximum effective sorption of Sr²⁺ over GO/Ni-MOF membrane is 32.99% with 2 mg composite membrane containing a high content of Ni-MOF at 299 K in 100 mg/L Sr²⁺ aqueous solution. The FT-IR and XPS results suggest that the synergistic effect between GO and Ni-MOF is determinant in the sorption Sr²⁺ process. The GO/Ni-MOF composite membrane is demonstrated to have the advantages of efficient removal of Sr²⁺, low cost and simple synthesis route, which is promising in the elimination of radionuclide contamination.

© 2020 The Author(s). Published by Elsevier B.V. on behalf of Chinese Society for Environmental Sciences, Harbin Institute of Technology, Chinese Research Academy of Environmental Sciences. This is an open access article under the CC BY-NC-ND license (<http://creativecommons.org/licenses/by-nc-nd/4.0/>).

1. Introduction

With the development of industry and the shortage of fossil fuel, nuclear energy advances rapidly and has attracted intense attention. However, the rapid development of nuclear power plants results in safety and environmental issues, particularly the removal and recovery of radionuclides from aqueous wastes [1,2]. Strontium (Sr) is one of the most hazardous radioactive contaminants that threaten the environment and human being. In particular, the ⁸⁹Sr isotope (t_{1/2} = 28 years) tend to deposited into human bones and result in bone sarcoma and leukemia, owing to its similar chemical property to calcium [3]. At this point, it is highly urgent to separate and recover the radioactive strontium ions from wastewaters with

an efficient method [4,5]. In the past decades, numerous technologies have been reported on this purpose, such as ion-exchange, adsorption, solvent extraction, and co-precipitation [5–10]. Among these available technologies, the adsorption over porous materials stands out as a simple and economical method owing to its none subsequent treatment request after the removal of strontium from the matrix [10]. Furthermore, the adsorption is also advantageous in its recyclability wherein the adsorbents can be regenerated easily [7,11]. In regard to adsorbents, the zeolites, polyacrylonitrile, and crystalline silicotitanate have been widely investigated in the removal of strontium ion (Sr²⁺) from groundwater, seawater, and/or nuclear waste solutions [6–9]. However, because of their high cost, low affinity towards strontium, and secondary contamination risk, the large-scale application of these adsorbents in Sr²⁺ removal is still far away [12]. Therefore, the seeking of an adsorbent with a high adsorption capacity and a fast adsorption rate is of the utmost importance for the removal of Sr²⁺ from aqueous solutions.

* Corresponding author.

** Corresponding author.

E-mail addresses: jieliang@buaa.edu.cn (J. Liang), gcshan@buaa.edu.cn (G. Shan).

Recently, the metal-organic frameworks (MOFs) with attractive characteristics of high surface area, tunable pores, and accessible coordinative unsaturated sites have drawn extensive multidisciplinary attention [13–21]. As an inorganic-organic hybrid porous material, MOFs have been applied in various research fields [19], such as heterogeneous catalysis [20,21], selective adsorption and/or separation [22,27–35], energy storage [23,26], gas storage [24] and biomedical applications [25,26]. Although several untreated MOF have been tested in Sr²⁺ adsorption, the results suggested that they exhibited limited adsorption capacity for Sr²⁺ and functional groups such as –COOH, –NH₂ and –X (halogen) are required for the linker functionalization to raise their affinity with Sr²⁺ ions. It should be noted that the post-functional steps not only complicated the synthesis routes of MOFs, it also significantly increased their synthesis cost. As a matter of fact, owing to their exceptional porosity and high surface area, water-stable MOFs could be used as effective adsorbents for the captures of metal ions [11,27–34,40–50].

In the present work, we reported the synthesis of MOF/graphene oxide (GO) composite membranes by suction filtration of electrostatic self-assembly Ni-MOF and GO sheets. The membranes not only possess interwove structures but also exhibit free-standing forms, which is greatly helpful for large-scale and repeated applications. Their strontium adsorption capacity is tested with the variation of contact time and initial concentrations, respectively, and the adsorption mechanisms towards Sr²⁺ are discussed.

2. Experimental

2.1. Synthesis of GO

GO nanosheets were synthesized via a modified Hummers' method by chemically exfoliating natural graphite flakes [11,36,41]. In a typical procedure, graphite flakes and sodium nitrates (NaNO₃) were slowly added into concentrated sulfuric acid (H₂SO₄) at room temperature. The mixture was then kept under ice bath at 0 °C with mild agitation. Potassium permanganate (KMnO₄) was gradually added in to the mixture while keeping the suspension temperature. Afterwards, the temperature of the mixed suspension was increased and kept until a thick paste was generated. After the brown mixture was turned into yellow, the mixture solution was diluted and added with H₂O₂ (30%). The final solution was centrifuged at 11,000 rpm till the pH of the system reached 7. The obtained sample was dried for further treatment.

2.2. Preparation of Ni-MOF nanobelts

44 mg of Ni(NO₃)₂·6H₂O (0.15 mmol) was dissolved in a 60 mL DMF/ethanol mixture (V_{DMF}: V_{ethanol} = 3:1), which was then treated by sonication to make it uniformly distributed. 1.56 mg of BPY (0.01 mmol) and 10.0 mg PVP were added to a vial with 6 mL of solution. 4.0 mg of TCPP was dissolved in a 2 mL DMF/ethanol mixture (V_{DMF}: V_{ethanol} = 3:1) and the dispersant was added into the above-mentioned mixture dropwise. The 8 mL mixture per vial was then treated by sonication for 10 min. Afterwards, the resulted mixture in vial was capped and transferred into an oven at 80 °C for 24 h. The final red product was washed by ethanol twice and separated by centrifugation (7500 rpm) for 20 min. Finally, 1D NiMOF nanobelts were obtained and re-dispersed in DMF.

2.3. Preparation of assembled Ni-MOF/GO composite membrane

The Ni-MOF/rGO electrode films were synthesized via an electrostatic self-assembly process. In a typical procedure, the GO dispersant in DMF (1 mg mL⁻¹) was slowly added into 20 mL of Ni-

MOF suspension (1 mg mL⁻¹) dropwise under stirring. The mixture was then subjected to continuous stirring for 1 h. Subsequently, the uniformly distributed GO/Ni-MOF dispersant was treated by vacuum filtration with organic membrane filters. Finally, the composite membrane was obtained after peeling off the filters and heated at 60 °C for 24 h in vacuum.

2.4. Characterization

The sample morphology was carried out on a field-emission scanning electron microscopy (SEM, Hitachi S-3400). Phase identification was measured by a powder X-ray diffractometer (PXRD, Bruker D8) with a Cu-K_α radiation. The X-ray photoelectron spectra (XPS) was performed on an ESCALAB250Xi spectrometer (ThermoFisher Co. Ltd). The concentration of Sr²⁺ was measured on an ESCALAB2000 analyzer by using the ICP method. IR spectra were measured on a Fourier transform infrared spectrometer (FTIR, Nicolet IS10) in the region of 4000–500 cm⁻¹.

2.5. Batch test

The experiments of Sr²⁺ adsorption over GO/Ni-MOF membranes were performed by batch tests. SrCl₂·6H₂O was used as the source of Sr²⁺. The tests were carried out under a constant oscillating speed of 250 rpm with 2 mg of GO/Ni-MOF membrane and 5 mL of Sr²⁺ aqueous solution. After the preset contact time, the membrane adsorbents were separated by centrifugation and dried at 60 °C in an oven. Subsequently, the concentration of strontium in the left solution was analyzed by ICP, and based on which the Sr²⁺ adsorption capacity and efficiency of GO/Ni-MOF membranes were calculated.

A series of adsorbents with various masses of Ni-MOF were studied for Sr²⁺ removal. The adsorption kinetics have been studied with the contact time of 30, 60, 120, 240, 480, 960 and 1440 min at room temperature (298 K). q_e (mg/g), the equilibrium Sr²⁺ adsorption capacity of GO/Ni-MOF membranes and the removal amount of Sr²⁺ per unit mass of membrane are calculated as follows:

$$q_e = \frac{(C_0 - C_e)V}{m} \quad (1)$$

where C_0 and C_e are initial and equilibrium concentrations in the supernatant (mg/L), respectively; m is the mass of the adsorbent (g) and V is the volume of the applied Sr²⁺ solution (L). The removal efficiency, RE (%), was given by:

$$RE = \frac{C_0 - C_e}{C_0} \times 100\% \quad (2)$$

A series of Sr²⁺ aqueous solutions with concentrations of 25, 50 and 100 mg/L were further studied for the Sr²⁺ removal over GO/Ni-MOF membranes. To fit the experimental adsorption data, Langmuir and Freundlich isotherm models were applied, respectively, based on the linear and non-linear regression [42]. The equation of Langmuir is given by:

$$q_e = \frac{Q_{0L}K_L C_e}{1 + K_L C_e} \times 100\% \quad (3)$$

where q_e (mg/g) is the adsorption amount of Sr²⁺ per unit mass of membrane, Q_{0L} indicated the maximum adsorption amount at a monolayer, C_e (mg/L) referred to the Sr²⁺ concentration at equilibrium, and K_L (L/mg) denoted the Langmuir constant that was related to the affinity of binding sites. The K_L and Q_{0L} values of can be obtained by fitting $1/C_e$ vs. $1/q_e$ following with the equation:

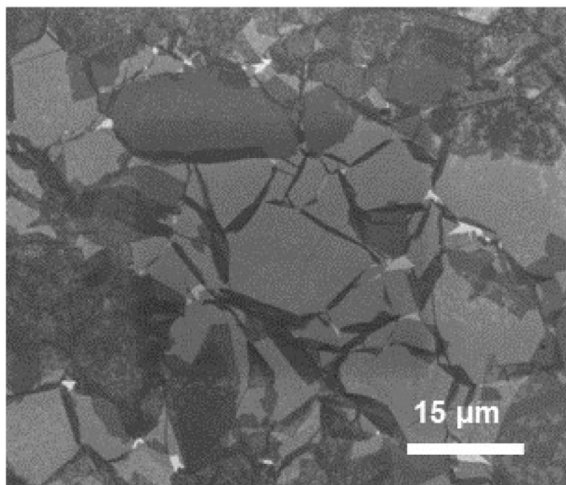


Fig. 1. (a) The TEM image of as-exfoliated GO nanosheets; (b) The statistical distribution of the sizes of GO nanosheets measured in the SEM images.

$$\frac{1}{q_e} = \frac{1}{Q_{01}} + \frac{1}{Q_{01}K_1C_e} \quad (4)$$

The equation of Freundlich isotherm model is given as follows:

$$\log q_e = \log k_{F1} + \frac{\log C_e}{n_{F1}} \quad (5)$$

where k_{F1} and $1/n_{F1}$ are measures of adsorption capacity and adsorption intensity, respectively.

3. Results and discussion

The GO and GO/Ni-MOF membranes were synthesized and thoroughly characterized, wherein GO was synthesized by chemically exfoliating the graphite *via* a modified Hummers' method [11]. Herein, the membrane consisting of GO was denoted as sample **G**, and the GO/Ni-MOF composite membranes with a low content (15 wt%) and a high content (35 wt%) of Ni-MOF were denoted as samples **G/N-15%** and **G/N-35%**, respectively. Similarly, the samples **1**, **L2**, **H3** after adsorption for 8, 24 and 24 h are denoted as samples **G-8hr**, **G/N-15%-24hr** and **G/N-35%-24hr**, respectively.

Fig. 1 shows that the as-exfoliated GO sheets have an average size of 8–9 μm . **Fig. 2a** shows the SEM image of Ni-MOF nanobelts, which is approximately 5–10 μm in length and ~300 nm in width. Parts of the nanobelts exhibit large thickness because of the

aggregation with each other. The XRD patterns in **Fig. 2b** manifests that the Ni-MOF particles are crystalline and exhibits a tetragonal crystal structure (inset of **Fig. 2b**). The simulated XRD pattern of the 1D Ni-MOF crystal based on the crystal structure ref. no. # 46-1623 in the JCPDS is also shown at the bottom of the plot. For the composite membrane **G/N-35%** containing a higher doping amount of Ni-MOF, the existence of the characteristic diffraction peaks of (112), (004) and (006) demonstrates that the Ni-MOF nanobelts maintain in the membranes. Furthermore, our previous work had confirmed that the XRD peak at 11.31° observed for GO could correspond to an interlayer spacing of $d = 7.81 \text{ \AA}$ for the graphene nanosheets [35]. Hence it is suggested the diffraction peak of (002) shifting from 11.3° for GO to 9.8° for **G/N-35%** membrane could be attributed to the insertion of MOF between neighboring graphene nanosheets.

The surface and cross-sectional morphology of samples in **Fig. 3a** indicates the interweave structure. On the other hand, it is observed that the Ni-MOF nanobelts uniformly penetrated GO layers structures (**Fig. 3a** and **b**), which can be attributed to the effective electrostatic self-assemble from intrinsically electronegative GO with oxygen-containing functional groups and intrinsically electropositive Ni-MOF with functional groups of metal ions [35]. The photographic image in a set of **Fig. 3b** demonstrates the flexibility and durability of composite membranes. **Fig. 4a, b, and c** show the morphology of samples **G**, **G/N-15%**, **G/N-35%** before adsorption, respectively. The membranes with a higher content of Ni-MOF can be observed to show gradually exposed Ni-MOF nanobelts, and the sample surface becomes extremely rough in sample **G/N-35%**. **Fig. 4d, e, and f** show the morphology of samples **G**, **G/N-15%**, **G/N-35%** after adsorption, respectively. Compared to those of samples before adsorption, the surface morphology of samples **G**, **G/N-15%**, **G/N-35%** after adsorption changes substantially, which seems to adhere with some Sr aggregations. Energy-dispersive X-ray spectrometry (EDX) mapping reveals successful Sr^{2+} adsorption over the GO/Ni-MOF membranes with different contents of Ni-MOF. As clearly shown in **Fig. 4g** and **h**, there are compositional distributions of C, Ni and Sr in samples **G/N-15%** and **G/N-35%**, respectively, suggesting that large amounts of Sr ions are immobilized in the composite membranes.

FTIR was performed to investigate the composition changes of composite membranes before and after Sr^{2+} adsorption. In **Fig. 5**, the peaks located at 1720, 1640, 1380, 1230, and 1040 cm^{-1} are ascribed to the vibration of C=O, carboxyl O=C-O, epoxy C-O-C, C-O, and C=C stretching, respectively [36]. In the spectrum of GO, the two broad bands centered at 3780 and 3060 cm^{-1} can be assigned to the O-H stretching originated from the physically adsorbed water vapor in the air. Although the peak located at

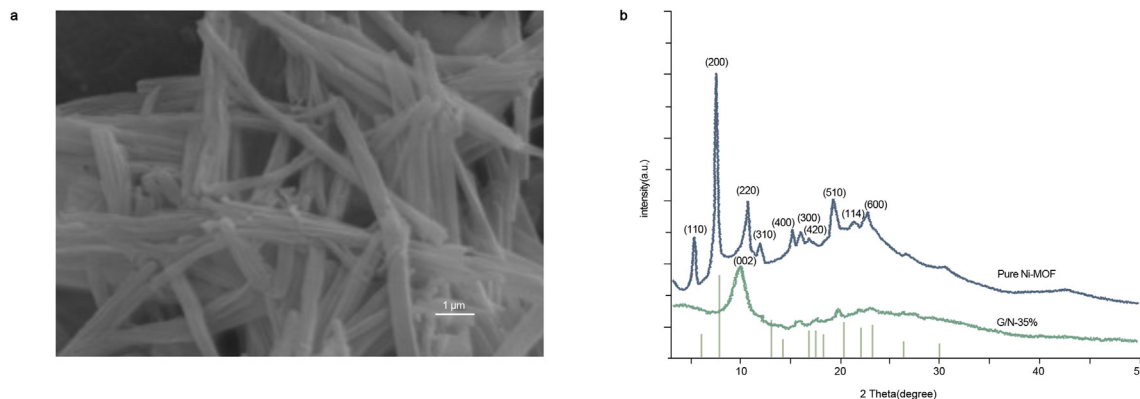


Fig. 2. (a) The SEM image of 1D Ni-MOF nanobelts; (b) The XRD patterns of 1D Ni-MOF nanobelts and the G/N-35% membrane.

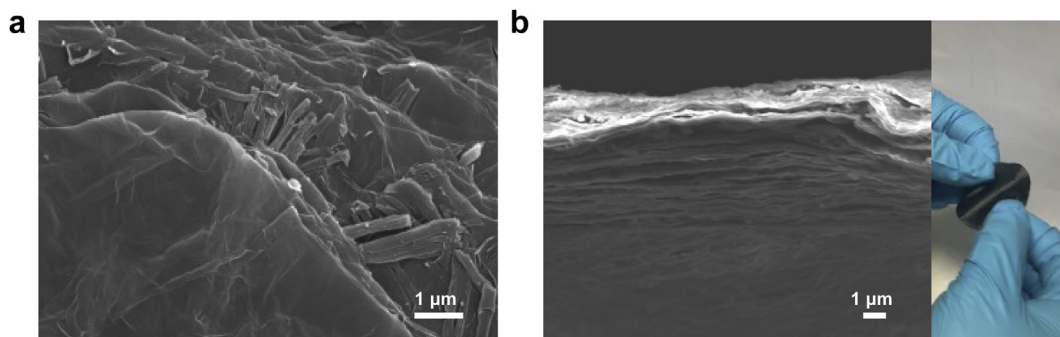


Fig. 3. (a, b and c) SEM image of samples G, G/N-15%, G/N-35% before adsorption; the inset shows their high-resolution SEM images before adsorption. (d, e and f) SEM image of samples G, G/N-15%, G/N-35% after adsorption; the inset shows their high-resolution SEM images after adsorption. (g) EDX elemental mapping images for sample G/N-15%. (h) EDX elemental mapping images for sample G/N-35%.

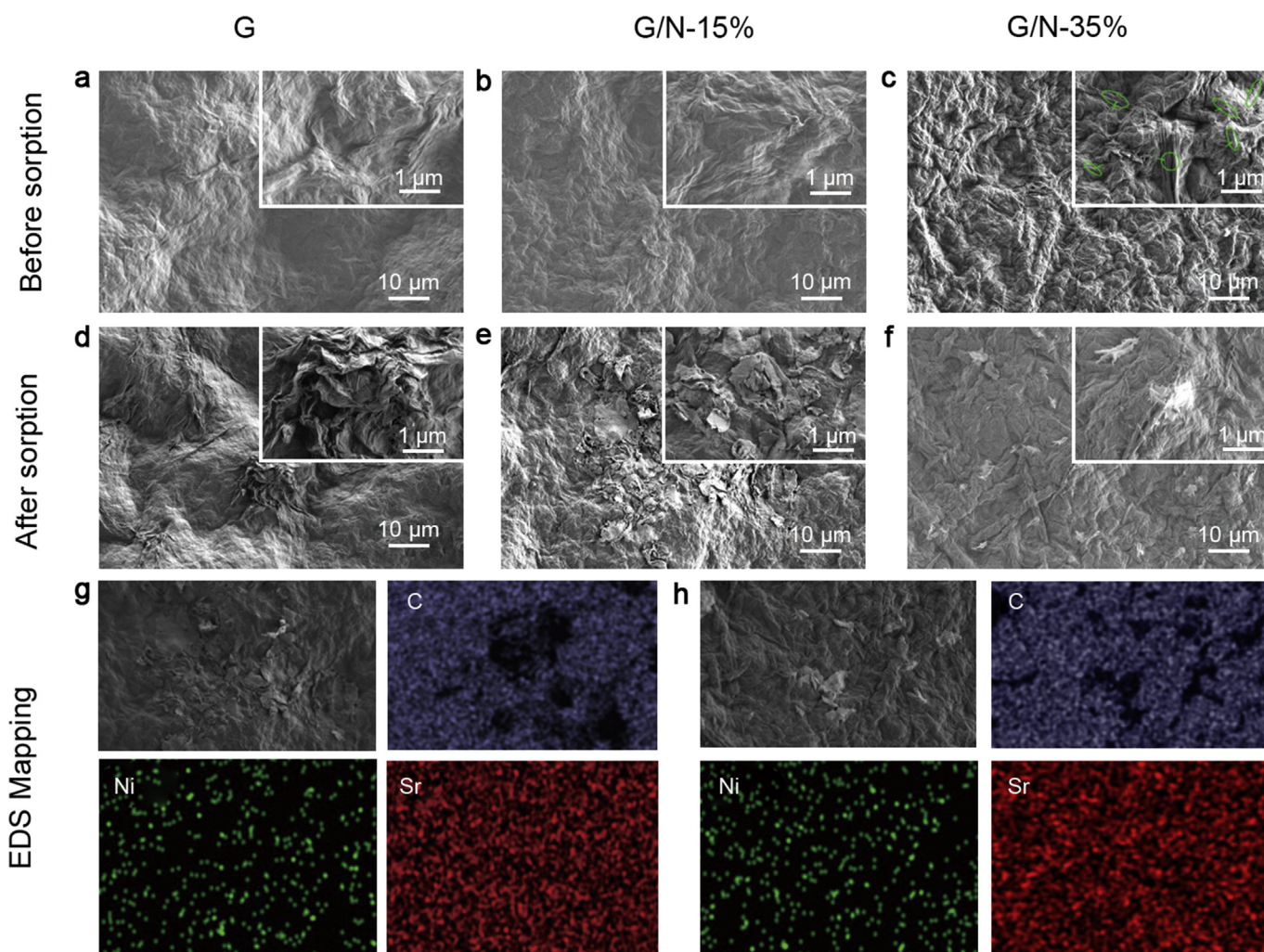


Fig. 4. (a) Surficial SEM image of composite membrane G/N-35%. (b) Cross-sectional SEM image of composite membrane G/N-35%. Inset is photographic image of flexible and freestanding GO/Ni-MOF membrane.

3460 cm^{-1} is also assigned to the O–H stretching in H_2O , such a water molecule is adsorbed at the MOF sites. In comparison, the peak centered at 3060 cm^{-1} is traced to the O–H stretching of H_2O , wherein the hydrogen is bonded to the displaced oxygen connecting to the linker. For the GO/Ni-MOF membrane, the broad

band appeared at 1630 cm^{-1} confirmed that the NiO_x clusters are attached to the surface of GO membrane *via* O-containing functional groups. After adsorption, the band at around 1630 cm^{-1} attributing to the vibration of carboxyl $\text{O}=\text{C}-\text{O}$ is shifted to 1590 cm^{-1} for sample G whereas its transmittance (%) is decreased

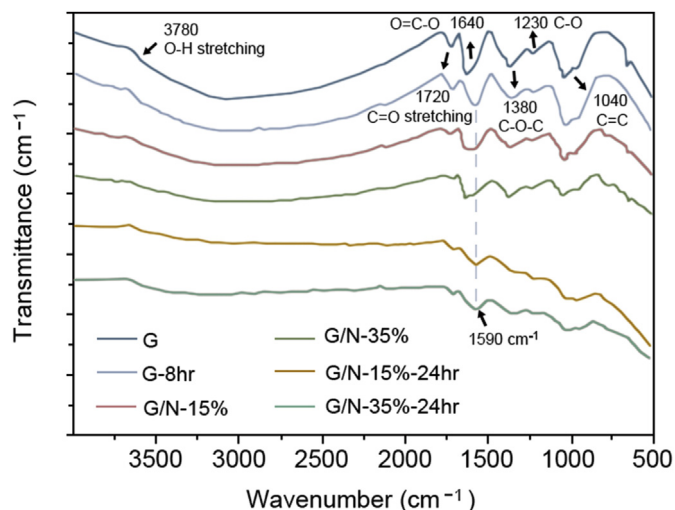


Fig. 5. FT-IR spectra of samples G, G-8, G/N-15%, G/N-15%-24hr, G/N-35% and G/N-35%-24hr.

Table 1
Kinetic parameters and linearity of fitting of pseudo-first-order and pseudo-second-order models for Sr²⁺ adsorption over samples G, G/N-15% and G/N-35%.

Samples	Pseudo-first-order model			Pseudo-second-order model		
	<i>k</i> ₁ (min ⁻¹)	<i>q</i> _e (mg/g)	R ²	<i>k</i> ₂ (g mg ⁻¹ min ⁻¹)	<i>q</i> _e (mg/g)	R ²
G	0.00399	59.92293	0.95794	5.49018E-05	72.6744186	0.99023
G/N-35%	0.02149	53.58634	0.92398	2.11E-04	65.35947712	0.99285
G/N-15%	0.00249	59.84533	0.81717	4.19608E-05	71.8907261	0.87983

Table 2
Comparison of the maximum adsorption capacity of strontium on Ni-MOF/GO membrane with other adsorbents.

Adsorbents	pH	Adsorption capacity (mg/g)	Reference
CHA zeolite	7.0	9.7	43
Natural clinoptilolite	7.0	9.8	44
Biogenic hydroxyapatite	7.0	34.2	45
Titanate nanofibers	7.0	55	46
Titanate nanotube	7.0	66	47
Ni-MOF/GO membrane	7.0	72	This study
Crystalline SilicoTitanates	7.0	174	48
zeolite A	7.0	271	49
GO-HAP	7.0	702.2	50

for samples G, G/N-15%-24hr and G/N-35%-24hr. This indicates that the O-containing functional groups in GO/Ni-MOF provide sufficient binding sites for strontium ions [37]. Take the sorption capacity into account, we make a comparison of the maximum adsorption capacity of strontium on Ni-MOF/GO membrane with other adsorbents in Table 2. The Ni-MOF/GO membrane exhibited a maximum sorption capacity of 72 mg/g for Sr²⁺ ions. Although the value is lower than those of benchmark zeolite A (271 mg/g) and Crystalline SilicoTitanates (174 mg/g), it is similar with those of CHA zeolite (66 mg/g), titanate nanotube (66 mg/g) and a titanate nanofiber (55 mg/g). In addition, compared to traditional adsorbents in the form of powder, the prepared Ni-MOF/GO in a membrane form would solve the problem of separation and recovery for fine particles, which is a major hurdle for industrial process. Therefore, the prepared Ni-MOF/GO membrane appeared as a promising strontium adsorbent candidate with a comparable adsorption capacity.

In order to reveal the adsorption mechanisms in the composite membranes, the adsorption kinetics is studied by fitting with the pseudo-first-order and pseudo-second-order models [32], respectively. These models are described by the following equations, respectively,

$$\ln(q_e - q_t) = \ln q_e - k_1 t \tag{6}$$

$$\frac{1}{q_t} = \frac{1}{k_2 q_e^2} + \frac{t}{q_e} \tag{7}$$

where *q*_e (mg g⁻¹) and *q*_{*t*} (mg g⁻¹) are the adsorption amounts of Sr²⁺ ions per mass of membrane at equilibrium and at a certain time *t* (min), respectively; *k*₁ (min⁻¹) and *k*₂ (g (mg min⁻¹)) refers to the rate constant in the pseudo-first-order and the pseudo-second-order models, respectively. Fig. 6 b-d depicted the fitting of Eq. (7) based on the pseudo-second-order model, while the related kinetic parameters are listed in Table 1. Compared with the linearity of fitting R² and the *q*_e values of the pseudo-first-order, it is obvious that the Sr²⁺ sorption kinetics over Ni-MOF or GO/Ni-MOF are better fitted with the pseudo-second-order model. Therefore, it is suggested that the rate of adsorption reaction is controlled by chemisorption. The Langmuir and Freundlich isotherms are further utilized to describe the Sr²⁺ adsorption behavior (Fig. 7). In general, the Langmuir model is applicable to a homogeneous adsorption surface where all adsorption sites have the same sorption energy independent of surface coverage, whereas the Freundlich isotherm model suggests a heterogeneous adsorption surface. Table S1 summarizes the relevant equilibrium adsorption amount *Q*_{OL}.

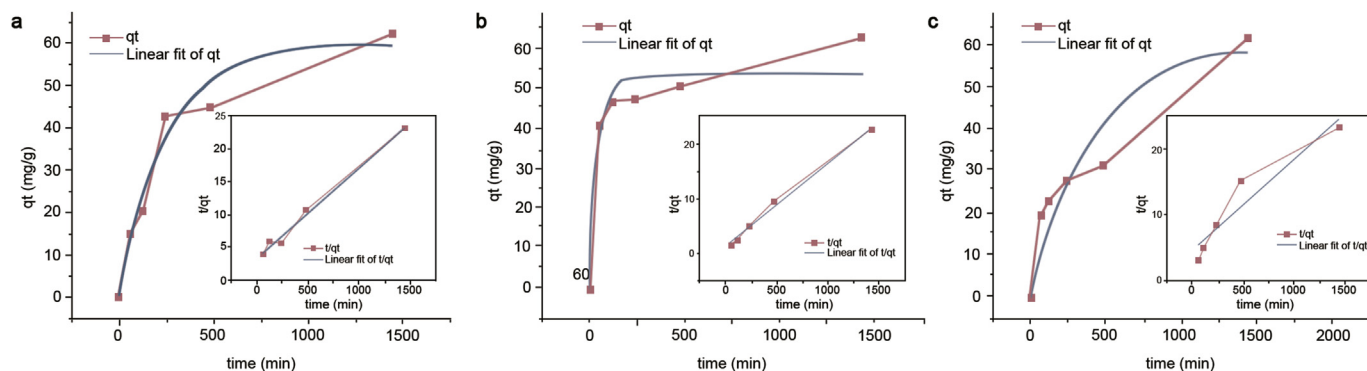


Fig. 6. (a) The related variation of Sr²⁺ uptake quantity on sample G. The inset shows the time-dependent sorption pseudo-second-order kinetic plots of Sr²⁺ removal over sample G. (b) The related variation of Sr²⁺ uptake quantity on G/N-35%. The inset shows the time-dependent sorption pseudo-second-order kinetic plots of Sr²⁺ removal over sample G/N-35%. (c) The related variation of Sr²⁺ uptake quantity on G/N-15%. The inset shows the time-dependent sorption pseudo-second-order kinetic plots of Sr²⁺ removal over sample G/N-15%.

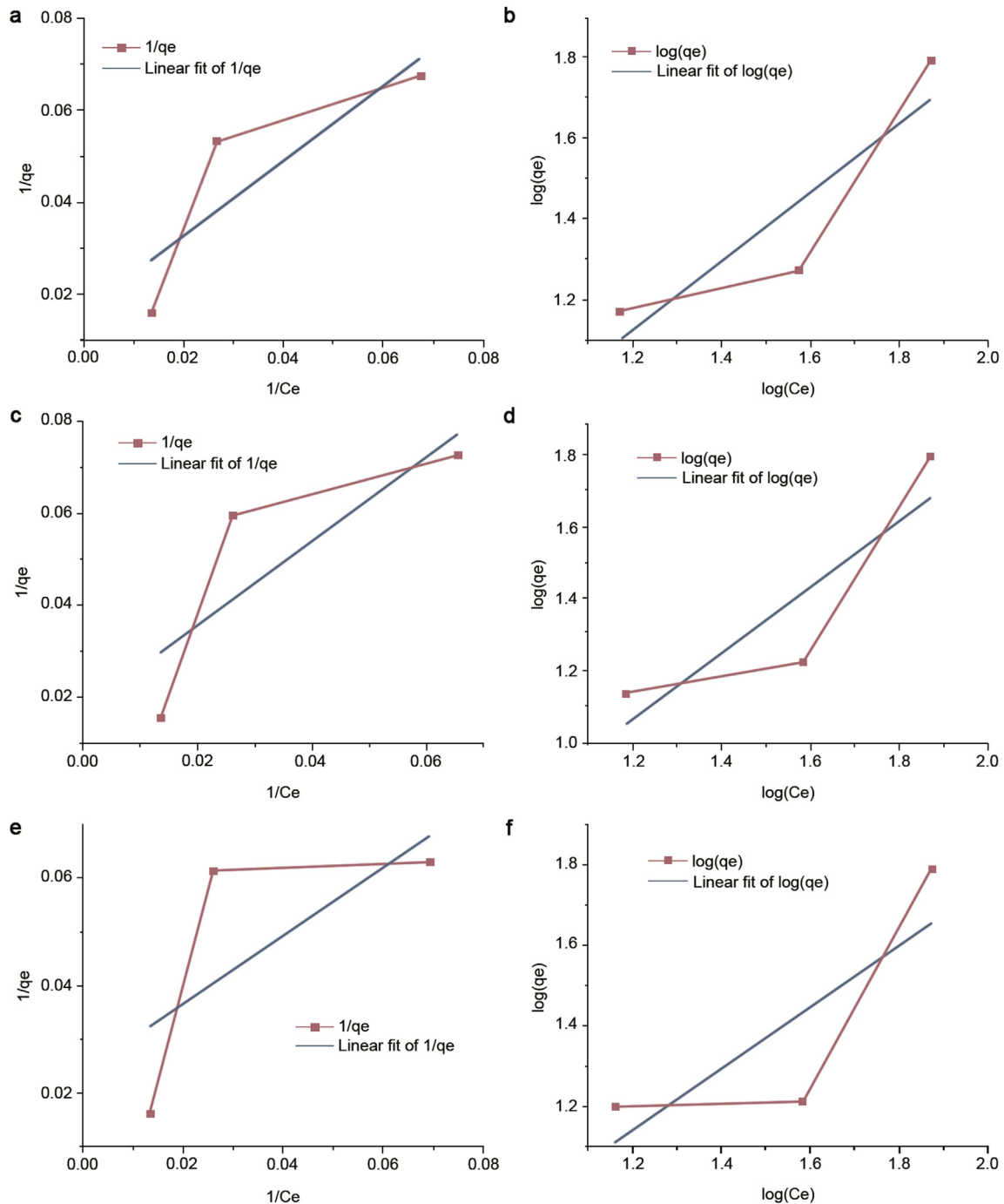


Fig. 7. (a) The sorption Langmuir kinetic plots for Sr^{2+} removal over sample G. (b) The sorption Freundlich kinetic plots for Sr^{2+} removal over sample G. (c) The sorption Langmuir kinetic plots for Sr^{2+} removal over sample G/N-35%. (d) The sorption Freundlich kinetic plots for Sr^{2+} removal over sample G/N-35%. (e) The sorption Langmuir kinetic plots for Sr^{2+} removal over sample G/N-15%. (f) The sorption Freundlich kinetic plots for Sr^{2+} removal over sample G/N-15%.

correlation coefficients, and related constants of the Langmuir and Freundlich isotherm models. Although both models well describe the Sr^{2+} adsorption isotherm, the Freundlich model is better fitted compared to the Langmuir model. This can be explained by the different adsorption energies raised from the adsorption sites located on the GO/Ni-MOF surface.

The contact time is a significant parameter that can be varied to determine the adsorption potential of an adsorbent. The adsorption of Sr^{2+} in a time period of 1~24 h at 299 K over samples are quantitatively measured (Fig. 8 a-c). The adsorbent dose is 2 mg;

The volume of solution is 5 mL, which has a Sr^{2+} concentration of 100 mg/L and 50 mg/L. As shown in Fig. 8a, the maximum Sr^{2+} removal efficiency for sample **G/N-35%** is 25.49% after adsorption for 24 h, which is close to those of samples **G** and **G/N-15%**. When samples **G** or **G/N-35%** are tested as adsorbents, the Sr^{2+} uptake increases significantly in the primary 1 h and is close to a saturation value after the adsorption for 4 h. As shown in Fig. 8b, the maximum Sr^{2+} removal efficiency of sample **G/N-35%** is 32.99% after the adsorption for 24 h, which is higher than those of samples **G** (26.67%) and **G/N-15%** (30.49%). From Fig. 8c, a huge change in

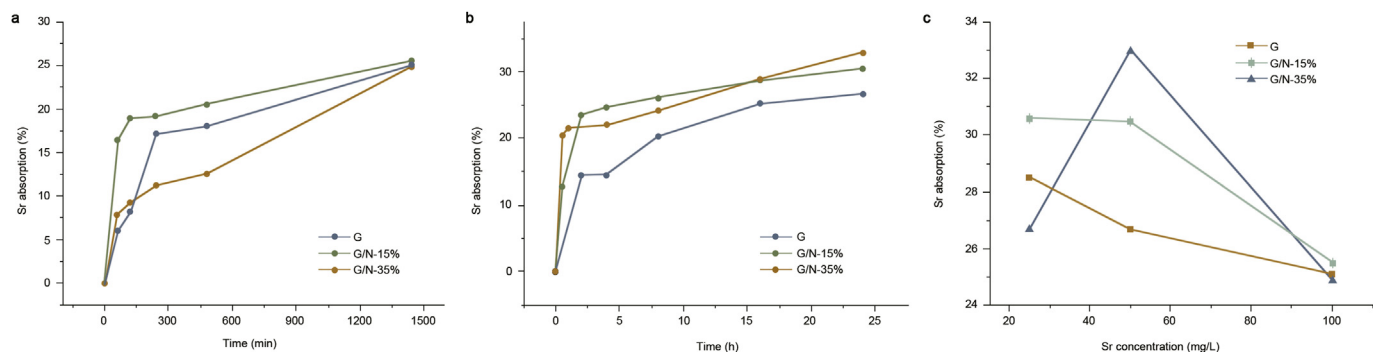


Fig. 8. (a) The effects of contact time on Sr²⁺ adsorption over samples G, G/N-15%, G/N-35% in the 100 mg/L Sr²⁺ solution; (b) Effects of contact time on Sr²⁺ adsorption over samples G, G/N-15%, G/N-35% in the 50 mg/L Sr²⁺ solution. (c) Effects of contact concentration on Sr²⁺ adsorption over samples G, G/N-15%, G/N-35%.

Sr²⁺ adsorption occurs for sample **G/N-15%** when the initial Sr²⁺ concentration was varied from 25 mg/L to 100 mg/L. The Sr²⁺ adsorption is 25.5% in the 100 mg/L Sr²⁺ solution while it is 30.6% in the 25 mg/L Sr²⁺ solution, suggesting that the composite membranes could exhibit different immobilization capacities when the Sr²⁺ ion concentration is varied in the solution.

High-resolution XPS scans for the overall C 1s and Sr 3d spectra were measured for the membranes before and after Sr²⁺ adsorption, with the aim to investigate the adsorption mechanisms of Sr²⁺ ions over the GO/Ni-MOF composites. An XPS

survey for sample **G/N-35%** after adsorption is presented in Fig. 9a–c. In Fig. 9b, the Sr²⁺ peak is observed in Sr²⁺ adsorbed GO/Ni-MOF, and the characteristic doublet peak of Sr 3d (133.98 eV, 135.68 eV) which are attributed to Sr 3d_{5/2} and Sr 3d_{3/2}, respectively, is evident. In the high-resolution C 1s spectra (Fig. 9c), the peaks can be deconvoluted into four peaks, which are assigned to the functional groups of C=C/C–C (284.7 eV), C–N (285.5 eV), O–C (286.5 eV), and C=O (288.2 eV), respectively. The presence of oxygen-containing metal-free groups (e.g., O–C=O, C=O) confirmed that abundant reactive sites existed in

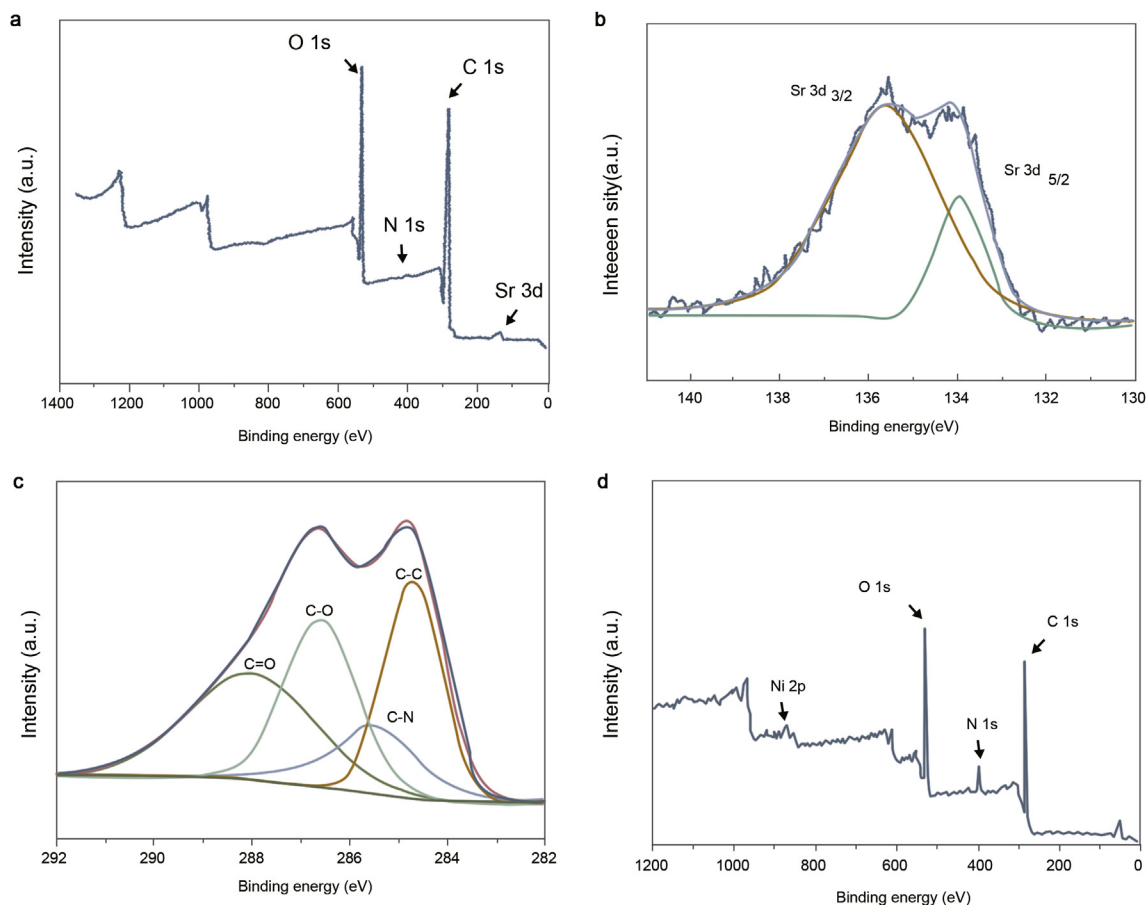


Fig. 9. (a) The XPS spectra of sample G/N-35%-24hr after Sr²⁺ sorption for 24 h. (b) The Sr 3d XPS spectrum of sample G/N-35%-24hr after Sr²⁺ sorption for 24 h. (c) The C1s XPS spectrum of sample G/N-35%-24hr after Sr²⁺ sorption for 24 h. (d) The XPS spectra of sample G/N-35%-24hr before Sr²⁺ sorption.

the composites for the binding of Sr^{2+} during the chemisorption processes. Additionally, the large surface area of porous MOF also provides sufficient spaces for the physical absorption of Sr^{2+} . These two kinds of sorption mechanisms had been confirmed by our previous work on the Cs^+ adsorption in the GO/Co-MOF composites [11]. Compared to that before Sr^{2+} sorption (Fig. 9d), no peak ascribed to nickel can be found in the overall spectrum after Sr^{2+} adsorption (Fig. 9a). This suggests that the Sr^{2+} ions may substitute Ni^{2+} ions in the Ni-MOF nanobelts, especially after considering the similar charge affinity for Sr^{2+} and Ni^{2+} ions. Therefore, except from the mechanisms of physical adsorption and chemisorption in the composites, it is envisaged that the substitutional effects of Sr^{2+} on the MOF structures are also responsible for the removal of Sr^{2+} ions from aqueous solution. Such a mechanism is further confirmed by morphology changes of the composite samples with plenty of exposed MOF

structures, as shown in Fig. 10a. That is, compared to the ordered rod-like morphology of Ni-MOF before adsorption, the MOFs in the composite after Sr^{2+} adsorption displays a rough surface. The newly generated pores in the MOF structure could be caused by the lattice deformation when Ni^{2+} is substituted by Sr^{2+} with a much larger ionic radius (Sr^{2+} : 0.125 nm; Ni^{2+} : 0.069 nm) [38]. More evidently, the EDS mapping also shows that there are large amounts of Sr^{2+} ions whereas very little Ni can be observed in the samples after adsorption (Fig. 10b). Furthermore, as shown in Fig. 10c, PXRD patterns of the samples after adsorption exhibited a new peak located at $2\theta = 22^\circ$, and the intensity of which increases with increasing Sr^{2+} absorption. This indicates that the strontium substitution slightly modified the crystal structure of MOF.

Based on the discussions above, it is suggested that there are three main mechanisms of Sr^{2+} adsorption in the GO/Ni-MOF

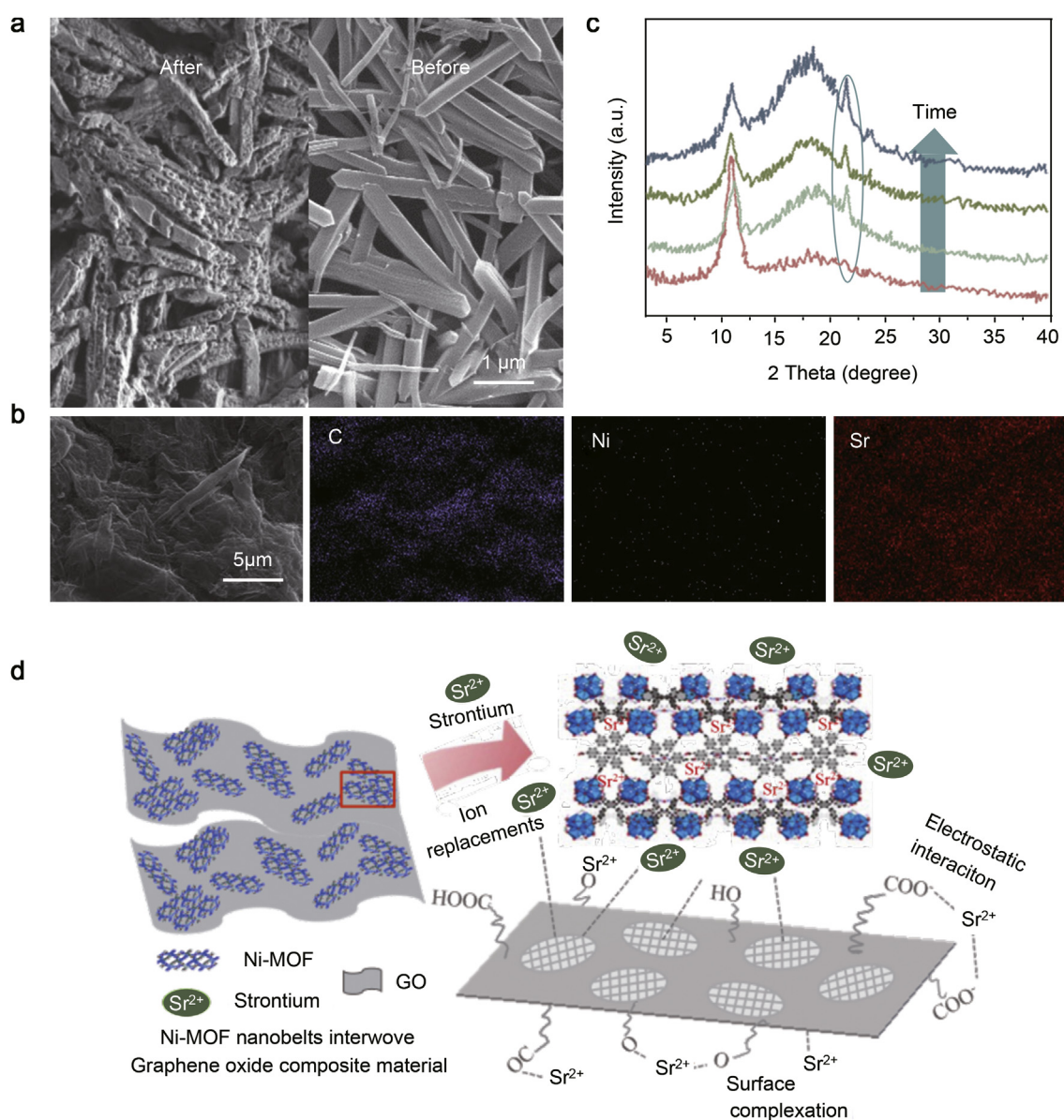
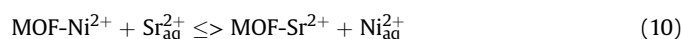
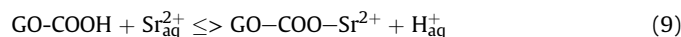
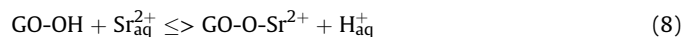


Fig. 10. (a) SEM images of the exposed Ni-MOF nanobelts in GO/Ni-MOF composite membranes before and after Sr^{2+} adsorption. (b) EDS mapping of GO/Ni-MOF composite membrane with exposed Ni-MOF nanobelts after Sr^{2+} adsorption. (c) XRD patterns of GO/Ni-MOF composite membranes with the highlighted peak whose intensity increases with increasing Sr^{2+} absorption time. (d) Schematic illustration of the immobilization of Sr^{2+} in the GO/Ni-MOF composite membranes.

composites, *i.e.*, the electrostatic interaction between Sr^{2+} with the oxygen-containing groups ($\text{O}-\text{C}=\text{O}$) and ($\text{C}=\text{O}$) in GO nanosheets, the physical absorption through the porous MOF structures and the GO-MOF interwove channels, and the substitution of Ni^{2+} with Sr^{2+} in the MOF structures, as shown schematically in Fig. 10d [39]. These mechanisms are considered to play individual roles in the removal of Sr^{2+} in aqueous solution. As a result of the Sr^{2+} adsorption in GO/Ni-MOF, H^+ ions are liberated from the solid surface and diffuse into the aqueous solution, which results in the formation of surface complexes, as follows:



On the other hand, the effective synergetic effect between MOF and GO also plays a pivotal role. It has also been reported that their in-plane oxygen functional groups can limit the water transport in graphene nano-channels because water could form hydrogen bonds with them, thereby rejecting Sr^{2+} in water into the GO channels, as illustrated in Fig. S1. Therefore, the GO membranes presented the worst Sr^{2+} absorption. For the GO/Ni-MOF membranes with sandwiched composite structures, however, the formation of interfaces between Ni-MOF and GO effectively eliminates hydrogen bonds at the GO surfaces, thus facilitating the permeation and absorption of Sr^{2+} with oxygen-containing groups in GO. On the other hand, the GO sheets also activate the surfaces of MOF structures, leading to the effective absorption of Sr^{2+} in Ni-MOF. Therefore, the synergistic effect of the unique architectures of GO and Ni-MOF can provide high specific surface area and facilitate the facile ion transfer and absorption in the GO/Ni-MOF membranes.

4. Conclusions

In summary, the self-assembled membranes consisting of MOFs and graphene oxides have been synthesized through a simple and facile high-yield filtration method. The existence of abundant oxygen-containing functional groups (*e.g.*, C-O, C=O) in the GO/Ni-MOF membranes is confirmed by FT-IR and XPS spectra. Batch experiments demonstrated that with a mass dose of 2 mg, the membrane with a high content of Ni-MOF has an optimal Sr^{2+} removal capacity after an adsorption time of 24 h, which is more efficient than bare GO and the membrane with a lower content of Ni-MOF. This work has demonstrated that the GO/Ni-MOF membranes presented here are a promising adsorbent candidate that can be used in the efficient removal of radioactive strontium from aqueous wastes.

Conflict of interest statement

The authors declare that they have no conflicts of interest.

Declaration of interests

The authors declare that they have no known competing financial interests or personal relationships that could have appeared to influence the work reported in this paper.

Acknowledgments

This work was supported by the National Key R&D Program of China (Grant No. 2016YFC1402504). Thanks to Dr. Jiefeng Gao at

Yangzhou University and Dr. Mingjun Hu at Beihang University as well as Prof. Xi Chen at Columbia University for helpful discussions.

Appendix A. Supplementary data

Supplementary data to this article can be found online at <https://doi.org/10.1016/j.ese.2020.100035>.

References

- [1] N.H. Abdullah, K. Shamel, E.C. Abdullah, L.C. Abdullah, Solid matrices for fabrication of magnetic iron oxide nanocomposites: synthesis, properties, and application for the adsorption of heavy metal ions and dyes, *Compos Part B* 162 (2019) 538–568.
- [2] W. Kuo, C. Pan, A reliability look at energy development, *Joule* 2 (1) (2017) 5–9.
- [3] D. Chakraborty, S. Maji, A. Bandyopadhyay, S. Basu, Biosorption of cesium-137 and strontium-90 by mucilaginous seeds of *Ocimum basilicum*, *Bio Technol.* 98 (15) (2007) 2949–2952.
- [4] M.J. Manos, M.G. Kanatzidis, Layered metal sulfides capture uranium from seawater, *J. Am. Chem. Soc.* 134 (2012) 16441–16446.
- [5] M.V. Balarama Krishna, S.V. Rao, J. Arunachalam, M.S. Murali, K. Surendra Kumar, V.K. Manchanda, Removal of ^{137}Cs and ^{90}Sr from actual low-level radioactive waste solutions using moss as a phyto-sorbent, *Separ. Purif. Technol.* 38 (2) (2004) 149–161.
- [6] K. Shakir, M. Sohah, M. Soliman, Removal of cesium from aqueous solutions and radioactive waste simulants by coprecipitate flotation, *Separ. Purif. Technol.* 54 (3) (2007) 373–381.
- [7] J. Liang, J. Li, X. Li, L. Wu, G.C. Shan, The sorption behavior of CHA-type zeolites for removing the strontium radionuclide from aqueous solutions, *Separ. Purif. Technol.* 230 (2019) 115874.
- [8] S. Singh, S. Eapen, V. Thorat, C.P. Kaushik, K. Raj, S.F. D'Souza, Phytoremediation of $^{137}\text{cesium}$ and $^{90}\text{strontium}$ from solutions and low level nuclear waste by *Vetiveria zizanioides*, *Ecotoxicol. Environ. Saf.* 69 (2) (2008) 306–311.
- [9] M.D. Neville, C.P. Jones, A.D. Turner, The EIX process for radioactive waste treatment, *Prog. Nucl. Energy* 32 (3) (1998) 397–401.
- [10] E.A. Abdelrahman, R.M. Hegazy, Exploitation of Egyptian insecticide cans in the fabrication of Si/Fenanostructures and their chitosan polymer composites for the removal of Ni(II), Cu(II), and Zn(II) ions from aqueous solutions, *Compos Part B* 166 (2019) 382–400.
- [11] J.Y. Cheng, J. Liang, L.B. Dong, J.X. Chai, Y.X. Jia, H. Wang, G.C. Shan, G.P. Zheng, Self-assembly of 2D-organic frameworks/graphene oxide membranes as highly efficient adsorbent for the removal of Cs^+ from aqueous solutions, *RSC Adv.* 8 (71) (2018) 40813–40822.
- [12] J. Jang, D.S. Lee, Enhanced adsorption of cesium on PVA-alginate encapsulated Prussian blue-graphene oxide hydrogel beads in a fixed-bed column system, *Bioresour. Technol.* 218 (2016) 294–300.
- [13] M. Bosch, S. Yuan, W. Rutledge, H.C. Zhou, Stepwise synthesis of metal-organic frameworks, *Acc. Chem. Res.* 50 (2017) 857–865.
- [14] A. Dhakshinamoorthy, A.M. Asiri, M. Alvaro, H. Garcia, Metal organic frameworks as catalysts in solvent-free or ionic liquid assisted conditions, *Green Chem.* 20 (2018) 86–107.
- [15] H. Furukawa, K.E. Cordova, M. O'Keeffe, O.M. Yaghi, The chemistry and applications of metal-organic frameworks, *Science* 341 (2013) 1230444.
- [16] P.A. Julien, C. Mottillo, T. Friscic, Metal-organic frameworks meet scalable and sustainable synthesis, *Green Chem.* 19 (2017) 2729–2747.
- [17] Z. Lin, J. Lv, M. Hong, R. Cao, Metal-organic frameworks based on flexible ligands (FL-MOFs): structures and applications, *Chem. Soc. Rev.* 43 (2014) 5867–5895.
- [18] H.C. Zhou, S. Kitagawa, Metal-organic frameworks (MOFs), *Chem. Soc. Rev.* 43 (2014) 5415–5418.
- [19] S. Zheng, X. Li, B. Yan, Q. Hu, Y. Xu, X. Xiao, H. Xue, H. Pang, Transition-metal (Fe, Co, Ni) based metal-organic frameworks for electrochemical energy storage, *Adv Energy Mater* 7 (18) (2017) 1602733–1602760.
- [20] C.F. Zhang, L.G. Qiu, F. Ke, Y.J. Zhu, Y.P. Yuan, G.S. Xu, X. Jiang, A novel magnetic recyclable photocatalyst based on a core-shell metal-organic framework $\text{Fe}_3\text{O}_4@\text{MIL}-100(\text{Fe})$ for the decolorization of methylene blue dye, *J. Mater. Chem.* 1 (45) (2013) 14329–14334.
- [21] J. Yu, C. Mu, B. Yan, X. Qin, C. Shen, H. Xue, H. Pang, Nanoparticle/MOF composites: preparations and applications, *Mater Horiz* 4 (2017) 557–569.
- [22] W. Zhang, F. Liang, C. Li, L.G. Qiu, Y.P. Yuan, F.M. Peng, X. Jiang, A.J. Xie, Y.H. Shen, J.F. Zhu, Microwave-enhanced synthesis of magnetic porous covalent triazine-based framework composites for fast separation of organic dye from aqueous solution, *J. Hazard Mater.* 186 (2011) 984–990.
- [23] J. Zhang, J. Xu, Y. Wang, H. Xue, H. Pang, Our contributions in nanochemistry for antibiotics, electrocatalyst and energy storage materials, *Chem. Rec.* 17 (2017) 1–15.
- [24] R. Banerjee, A. Phan, B. Wang, C. Knobler, H. Furukawa, M. O'keeffe, O.M. Yaghi, High-throughput synthesis of zeolitic imidazolate frameworks and application to CO_2 capture, *Science* 319 (2008) 939–943.
- [25] S. Zheng, H. Xue, H. Pang, Supercapacitors based on metal coordination

- materials, *Coord. Chem. Rev.* 373 (2017) 2–21.
- [26] Y. Yang, Q. Hu, Q. Zhang, K. Jiang, W. Lin, Y. Yang, Y. Cui, G. Qian, A large capacity cationic metal–organic framework nanocarrier for physiological pH responsive drug delivery, *Mol. Pharm.* 13 (2016) 2782–2786.
- [27] I. Ahmed, S.H. Jhung, Applications of metal–organic frameworks in adsorption/separation processes via hydrogen bonding interactions, *Chem. Eng. J.* 310 (2017) 197–215.
- [28] J.B. Decoste, G.W. Peterson, Metal–organic frameworks for air purification of toxic chemicals, *Chem. Rev.* 114 (2014) 5695–5727.
- [29] Z. Hasan, S.H. Jhung, Removal of hazardous organics from water using metal–organic frameworks (MOFs): plausible mechanisms for selective adsorptions, *J. Hazard Mater.* 283 (2015) 329–339.
- [30] N.A. Khan, S.H. Jhung, Adsorptive removal and separation of chemicals with metal–organic frameworks: contribution of p-complexation, *J. Hazard Mater.* 325 (2017) 198–213.
- [31] P.W. Seo, J.Y. Song, S.H. Jhung, Adsorptive removal of hazardous organics from water with metal–organic frameworks, *Appl. Chem. Eng.* 27 (2016) 358–365.
- [32] J. Wen, Y. Fang, G.M. Zeng, Progress and prospect of adsorptive removal of heavy metal ions from aqueous solution using metal–organic frameworks: a review of studies from the last decade, *Chemosphere* 201 (2018) 627–643.
- [33] P.A. Kobielska, A.J. Howarth, O.K. Farha, S. Nayak, Metal–organic frameworks for heavy metal removal from water, *Coord. Chem. Rev.* 358 (2018) 92–107.
- [34] Y. Ming, J. Purewal, J. Yang, C.C. Xu, R. Soltis, J. Warner, M. Veenstra, M. Gaab, U. Muller, D.J. Siegel, Kinetic stability of MOF-5 in humid environments: impact of powder densification, humidity level, and exposure time, *Langmuir* 31 (17) (2015) 4988–4995.
- [35] J.Y. Cheng, J. Liang, L.B. Dong, J.X. Chai, N. Zhao, S. Ullah, H. Wang, D.Q. Zhang, S. Imtiaz, G.C. Shan, G.P. Zheng, *RSC Adv.* 8 (2018) 40813–40822.
- [36] J.Y. Cheng, S.M. Chen, D. Chen, L.B. Dong, J.J. Wang, T.L. Zhang, T.P. Jiao, B. Liu, H. Wang, J.J. Kai, D.Q. Zhang, G.P. Zheng, L.J. Zhi, F.Y. Kang, W.J. Zhang, Editable asymmetric all-solid-state supercapacitors based on high-strength, flexible, and programmable 2D-metal–organic framework/reduced graphene oxide self-assembled papers, *J. Mater. Chem.* 6 (2018) 20254–20266.
- [37] Y. Ming, J. Purewal, J. Yang, C.C. Xu, Kinetic stability of MOF-5 in humid environments: impact of powder densification, humidity level, and exposure time, *Langmuir* 31 (17) (2015) 4988–4995.
- [38] W.J. Mu, S.Z. Du, X.L. Li, Q.H. Yu, R. Hu, H.Y. Wei, Y.C. Yang, S.M. Peng, Efficient and irreversible capture of strontium ions from aqueous solution using metal–organic frameworks with ion trapping groups, *Dalton Trans.* 48 (2019) 3284–3290.
- [39] Y. Marcus, Ionic radii in aqueous solutions, *Chem. Rev.* 88 (1988) 1475–1498.
- [40] T. Wen, X.L. Wu, M.C. Liu, Z.H. Xing, X.K. Wang, A.W. Xu, Efficient capture of strontium from aqueous solutions using graphene oxide–hydroxyapatite nanocomposites, *Dalton Trans.* 43 (2014) 7464–7472.
- [41] Z. Han, K. Zhan, X.Y. Wang, G.P. Zheng, J.H. Yang, Scalable piezoelectricity in graphene oxide papers tuned by hydrogen bonds, *Adv. Electron. Mater.* 2 (2016) 1600224.
- [42] A.O. Dada, A.P. Olalekan, A.M. Olatunya, O. Dada, *Langmuir*, Freundlich, Temkin and Dubinin–Radushkevich isotherms studies of equilibrium sorption of Zn²⁺ onto phosphoric acid modified rice husk, *IOSR J. Appl. Chem.* 3 (2012) 38–45.
- [43] J. Liang, J. Li, X. Li, L. Wu, G.C. Shan, The sorption behavior of CHA-type zeolites for removing the strontium radionuclide from aqueous solutions, *Separ. Purif. Technol.* 230 (2020) 115874.
- [44] I. Smičiklas, S. Dimović, I. Plečaš, Removal of Cs¹⁺, Sr²⁺ and Co²⁺ from aqueous solutions by adsorption on natural clinoptilolite, *Appl. Clay Sci.* 35 (2007) 139–144.
- [45] S. Handley-Sidhu, J.C. Renshaw, S. Moriyama, B. Stolpe, C. Mennan, S. Bagheriasl, P. Yong, A. Stamboulis, M. Paterson-Beedle, K. Sasaki, R.A.D. Patrick, J.R. Lead, L.E. Macaskie, Uptake of Sr²⁺ and Co²⁺ into biogenic hydroxyapatite: implications for biomineral ion exchange synthesis, *Environ. Sci. Technol.* 45 (2011) 6985–6990.
- [46] D. Yang, Z. Zheng, H. Liu, H. Zhu, X. Ke, Y. Xu, D. Wu, Y. Sun, Layered titanate nanofibers as efficient adsorbents for removal of toxic radioactive and heavy metal ions from water, *J. Phys. Chem. C* 112 (2008) 16275–16280.
- [47] D. Yang, S. Sarina, H. Zhu, H. Liu, Z. Zheng, M. Xie, S.V. Smith, S. Komarneni, Capture of radioactive cesium and iodine ions from water by using titanate nanofibers and nanotubes, *Angew. Chem., Int. Ed. Engl.* 50 (2011) 10594–10598.
- [48] O. Oleksienko, I. Levchuk, M. Sitarz, S. Meleshevych, V. Strelko, M. Sillanpää, Removal of strontium Sr²⁺ from aqueous solutions with titanate-silicate-sobtained by the sol-gel method, *J. Colloid Interface Sci.* 438 (2015) 159–168.
- [49] R.O. Abdel Rahman, H.A. Ibrahim, M. Hanafy, N.M. Abdel Monem, Assessment of synthetic zeolite Na A-X as sorbing barrier for strontium in a radioactive disposal facility, *Chem. Eng. J.* 157 (2010) 100–112.
- [50] T. Wen, X.L. Wu, M.C. Liu, Z.H. Xing, X.K. Wang, A.W. Xu, Efficient capture of strontium from aqueous solutions using graphene oxide–hydroxyapatite nanocomposites, *Dalton Trans.* 43 (2014) 7464–7472.